

45% Periodicity Reduction in Nanocomposite Thin Films via Rapid Solvent Removal

Jingyu Huang, Xiangfan Chen, Peter Bai, Rihan Hai, Cheng Sun and Ting Xu*

SUPPORTING INFORMATION

EXPERIMENTAL SECTION

Optical property measurements. Samples were spin-casted on cover glass slide in the dimension of 1 inch \times 1 inch. Reflection ellipsometry experiment was conducted using a spectroscopic ellipsometer (M2000U, J.A. Woollam) to measure the complex refractive index of the as-cast and annealed supramolecular nanocomposite thin films. The white light source used had a broad spectrum of wavelength ranging from 250 to 1000 nm. Biaxial model was used to retrieve the refractive index of the samples.

Angle resolved transmission measurements. The transmission spectra of the samples were characterized using angle-resolved optical spectroscopy combined with an inverted optical microscope (Leica DMI 3000M microscope) and a matching grating spectrometer (SR-303i, Andor Technology).¹ A high numerical aperture (NA) objective lens (50x, NA = 0.8) was used to collect all the light propagating through the sample, with a maximum incident angle determined by the condenser's NA (NA = 0.55). A 100 W halogen lamp was used as the illumination source, while a rotating linear polarizer (LPVISB100, Thorlabs) was used to control the polarization of the incident light. The transmission spectra were normalized with respect to the bare glass substrate.

SI 1. Thin Film Swelling and Drying Profiles during SVA and Rapid Solvent Removal

Thin films samples were treated with solvent annealing under chloroform vapor. The swelling and drying profile is plotted as the solvent volume fraction in the film vs. annealing time.

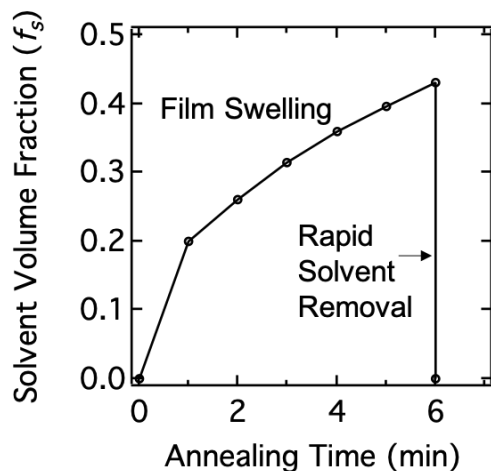


Figure S1. A typical thin film swelling and drying profile indicating solvent volume fraction f_s vs. annealing time.

SI 2. Nanoparticle Size Analysis

Size analysis of the nanoparticles used in the experiments were conducted based on multiple TEM images. Au NPs are coated by oleylamine. Fe_2O_3 NPs are coated by oleic acid.

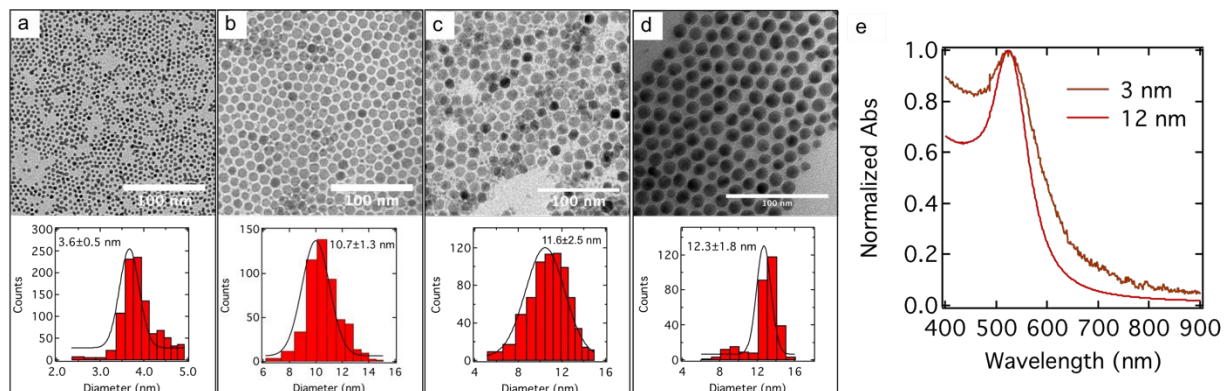


Figure S2. TEM images and size analysis of (a) 3 nm Au NPs, (b) 10 nm and (c) 12 nm Fe_2O_3 NPs, (d) 12 nm Au NPs. (e) Normalized absorption spectra of 3 and 12 nm Au NPs dispersed in chloroform.

SI 3. Calculation and Analysis of the Dispersion Relation of the Polariton Modes in 3-D Plasmonic Crystals

The plasmonic crystal model investigated here is composed of Au NPs periodically embedded in polymer matrix with permittivity $\varepsilon_h = 2.43$ as illustrated in Figure 1a. The diameter of an individual Au NP is about 3 nm or 12 nm, and the center-to-center distance along the z-direction is determined by the lamellae periodicities, which are 20 nm and 41 nm. In xy-plane, the inter-particle gap is kept constant as 3 nm. Noting that the fields inside the metal sphere are supposed to be homogenous since the radius is smaller than the skin depth (22 nm), and the quantum effect can be ignored in this size.² Thus, the Au NPs can be treated as the plasmonic “atoms” and permit the use of previously reported classic dipole coupling model.^{2,3} Prior to studying the inter-particle coupling, the intrinsic resonant frequency of a single Au NP is determined to be $\omega_0 = 3.63 \times 10^{15} \text{ rad/s}$ (corresponds to a resonance centered at 520 nm), which is based on the experimental data for the Au NPs in chloroform solution. For the polariton mode that induced by the coupling effect between the photons and the long transverse plasmon wave, the fundamental equations governing the coupling effect in the plasmonic crystal can be derived similar as an ionic crystal, and the effective dielectric function can be subsequently obtained from the previously reported dipole coupling model.³

To better understand the coupled phenomena in the 3-D array of electric dipoles, we first consider the interaction of two electric dipole moments \vec{P}_j and \vec{P}_k with the relative position vector \vec{r}_{jk} (Figure S2a). The quasi-static interaction energy V is given by

$$V = -\frac{1}{4\pi\varepsilon_0 r_{jk}^3} [3(\vec{P}_j \cdot \hat{e}_{jk})(\vec{P}_k \cdot \hat{e}_{jk}) - (\vec{P}_j \cdot \vec{P}_k)]$$

in which \hat{e}_{jk} is a unit vector parallel to the position vector \vec{r}_{jk} .⁴ In our case, the electric dipoles with uniform magnitude P are all aligned along the electric field of the incidence and thus, the equation can be further simplified to

$$V = \gamma \frac{\vec{P}_j \cdot \vec{P}_k}{4\pi\epsilon_0 r_{jk}^3} = \gamma \frac{P^2}{4\pi\epsilon_0 r_{jk}^3}$$

in which the interaction index γ is +1 and -2 for the case of transverse coupling (TC) and longitudinal coupling (LC), respectively. The energy-levels of the hybridization model of two coupled electric dipoles ($|\omega_0\rangle$) are illustrated in Figure S2b. In the symmetric LC (*s-LC*) hybridized state $|\omega_{-s-LC}\rangle$, the attraction of the opposite poles decreases the restoring force and therefore leads to the redshift of resonant frequency; while the antisymmetric LC (*a-LC*) hybridized state $|\omega_{+a-LC}\rangle$ leads to the blueshift of resonant frequency due to the increasing restoring force. In contrast, the corresponding frequency shifts are reversed in the case of the transverse coupling. The symmetric TC (*s-TC*) hybridized state $|\omega_{+s-LC}\rangle$ and antisymmetric TC (*a-TC*) hybridized state $|\omega_{-a-LC}\rangle$ result in the blueshift and redshift of the resonance frequency, respectively.

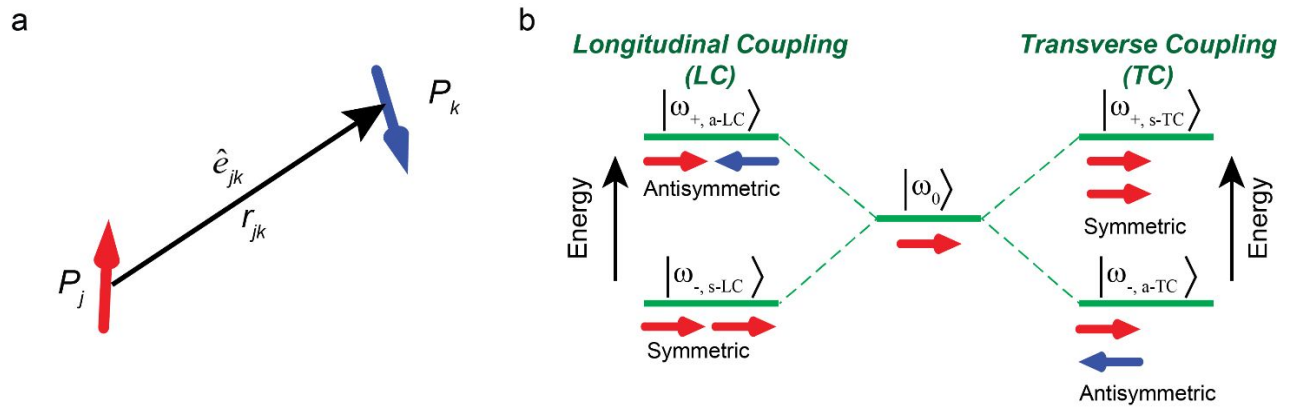


Figure S3. (a) The interaction between two dipoles moments \vec{P}_j and \vec{P}_k with \vec{r}_{jk} as the center-to-center vector. (b) Schematic illustration of energy-levels for symmetric and antisymmetric arrangements of *LC* and *TC* cases.

In the 3-D plasmonic crystal, the symmetric arrangement of both TC and LC modes coexist and compete mutually to determine the collective Eigen mode, as described in Table S1. For clarity, the in-plane interaction distance is defined as $r_{in} = 6$ nm or 15 nm for 3 nm or 12 nm Au NPs, respectively, which is much smaller than the out-of-plane interaction distance $r_{out} = 20$ nm or 41 nm determined by the lamellar periodicities.

Table S1. Collective energy level of different coupling modes.

Cases	Parallel Case ($\theta = 0^\circ$)			Normal Case ($\theta = 90^\circ$)		
Direction	In-plane		Out-of-plane	In-plane		Out-of-plane
Modes	<i>s-TC</i>	<i>s-LC</i>	<i>s-TC</i>	<i>s-TC</i>	<i>s-TC</i>	<i>s-LC</i>
V	$1 \frac{P^2}{4\pi\epsilon_0 r_{in}^3}$	$-2 \frac{P^2}{4\pi\epsilon_0 r_{in}^3}$	$1 \frac{P^2}{4\pi\epsilon_0 r_{out}^3}$	$1 \frac{P^2}{4\pi\epsilon_0 r_{in}^3}$	$1 \frac{P^2}{4\pi\epsilon_0 r_{in}^3}$	$-2 \frac{P^2}{4\pi\epsilon_0 r_{out}^3}$
	Collective energy level < 0 , redshift			Collective energy level > 0 , blueshift		

SI 4. Angle-resolved Transmission Spectra of Nanocomposite Thin Films with 3 nm Au NPs

In the presence of strong interparticle coupling, coupling between the propagating light wave and the transverse particles plasmon wave results in the polaritonic stop band.² Lamellar Au NPs assemblies shown in Figure S4a have both in-plane and out-of-plane coupling modes. The relative coupling strength between two adjacent NPs as a function of the ratio between interparticle gap and particle diameter is calculated using the discrete dipole approximation (DDA) method⁵ (Figure S4b). The in-plane coupling between 12 nm NPs is very strong but weak for 3 nm NPs. However, with the large interparticle distance across neighboring lamellae (~41 nm), there is negligible out-of-plane coupling. To engage effective out-of-plane coupling, it requires significant reduction of the lamellar periodicity (L). We calculated the polariton dispersion³ for 12 nm NPs, but significantly reduced lamellar periodicity by half to 20 nm in Figure S4c. The center wavelength of the polariton bandgap shows a pronounced blueshift from 572 nm (red dash line) for the light wave propagating along z -direction ($\theta = 0^\circ$) to 534 nm (blue dash line) for the light wave propagating along the orthogonal direction ($\theta = 90^\circ$). The results justify the possibility to reach strongly coupled region and to manipulate wavelength-dependent optical anisotropy of NP assemblies with high sensitivity.

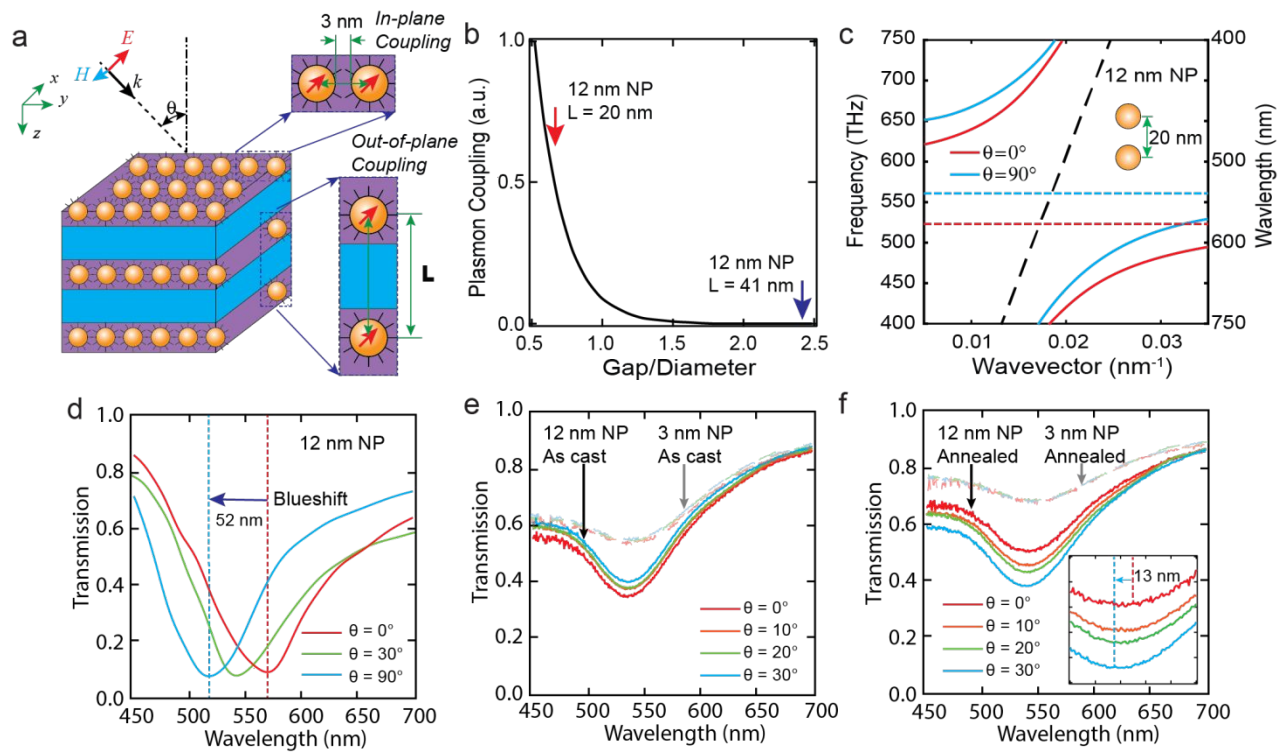


Figure S4. Angular- and wavelength-dependent optical properties of the nanocomposite thin films. (a) Schematic illustration of the lamellar nanocomposite film. (blue: PS; purple: P4VP(PDP); orange: NP) (b) Calculated relative plasmon coupling strength between two neighboring Au NPs as a function of the ratio between interparticle gap and particle diameter. (c) Calculated dispersion relations of the nanocomposite containing 12 nm Au NPs with the lamellar periodicity of 20 nm. (d) Calculated transmission spectra of annealed thin film containing 12 nm Au NPs. (e, f) Experimentally measured angle-resolved transmission spectra of 140 nm (e) as cast and (f) annealed films containing 9 vol% of 3 nm (dashed lines) or 12 nm (solid lines) Au NPs.

Figure S4d shows the angular-dependent transmission spectra of the nanocomposite film containing 12 nm Au NPs with a lamellar periodicity of 22 nm calculated numerically using the FDTD method. (FDTD Solution, Lumerical Inc.) The center wavelengths of the transmission

minimums exhibit a pronounced blueshifts from 570 nm to 518 nm when changing the incident angle from 0° to 90°, in good agreement with the theoretical calculation in Figure S4c. Transmission spectra of 140 nm nanocomposite thin films with 9 vol% of 12 nm Au NPs were measured with angle-resolved optical spectroscopy.¹ The as cast film in Figure S4e comprises an amorphous arrangement of Au NPs. The transmission spectra of the as cast film show angle-independent response with the transmission minimum remaining unshifted at the center wavelength of 538 nm. However, the transmission minimum of the annealed film in Figure S4f containing 12 nm Au NP lamellae blueshifts from 549 nm to 536 nm as the incident angle changes from 0° to 30°. This trend is in good agreement with the simulated result in Figure S4d. In comparison, despite its structural anisotropy, the measured transmission spectra of both as cast and annealed thin films containing 9 vol% of 3 nm Au NPs show very similar angle-independent transmission from 0° to 30° (Figure S4e and S4f) due to the weak interparticle couplings between those small NPs as expected. Thus, the macroscopic optical properties of nanocomposite thin film with the same composition can be tuned by the NP size and special organization.

SI 5. Wavelength and NP Size-dependent Optical Anisotropy in Nanocomposite Thin Films

Refractive indices of thin films of PS(40 kDa)-*b*-P4VP(5.6 kDa)(PDP)₁ supramolecule were measured. No obvious optical anisotropy in the visible light region of is observed.

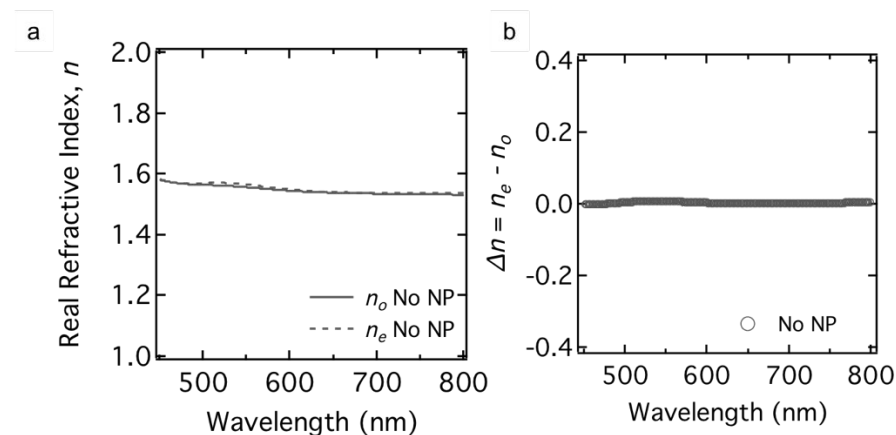


Figure S5. Wavelength and NP size-dependent optical anisotropy in 140 nm PS(40 kDa)-*b*-P4VP(5.6 kDa)(PDP)₁ thin films. (a) Ellipsometry measurements of the in-plane (n_o) and out-of-plane (n_e) components of the real refractive indices. (b) Difference of the out-of-plane (n_e) and in-plane (n_o) real refractive indices calculated from (a).

A series of 140 nm supramolecular thin films containing 9 vol% of 3 nm and 12 nm Au NPs before and after solvent annealing are used to investigate NP size-dependent optical properties of the nanocomposites. NPs were randomly distributed in the as cast films but well-ordered in lamellar structures in the annealed films. The real part of the in-plane refractive index (n_o) and out-of-plane refractive index (n_e) of as cast and annealed films were measured by ellipsometry (Figure S4a) and plotted in Figure S4b, d to characterize the optical anisotropy. For the solvent annealed films, the in-plane inter-particle gap is 3 nm, much smaller than the out-of-plane gap of 22 nm, thereby leading to a stronger inter-particle plasmonic coupling in-plane than

out-of-plane to the first approximation as discussed above. Consequently, a wavelength-dependent optical anisotropy was observed between 450 and 700 nm and Δn , the difference between n_e and n_o , were plotted in Figure S4c, e. In detail, Δn of the annealed films is larger than the as cast films with the same compositions (Figure S4c, e), and Δn of films with 12 nm Au NPs is much larger than films with 3 nm Au NPs, especially below 600 nm. In summary, for the solvent annealed films, 3 nm Au NPs show small optical anisotropy and is relatively independent on NP arrangements; but 12 nm Au NPs show obvious wavelength-dependent optical anisotropies and depend obviously on NP arrangements due to the relatively strong dipole coupling in both of in-plane and out-of-plane directions. Therefore, the results demonstrate the potential to manipulate the optical properties of the 3-D plasmonic crystal using lamellar supramolecular nanocomposites.

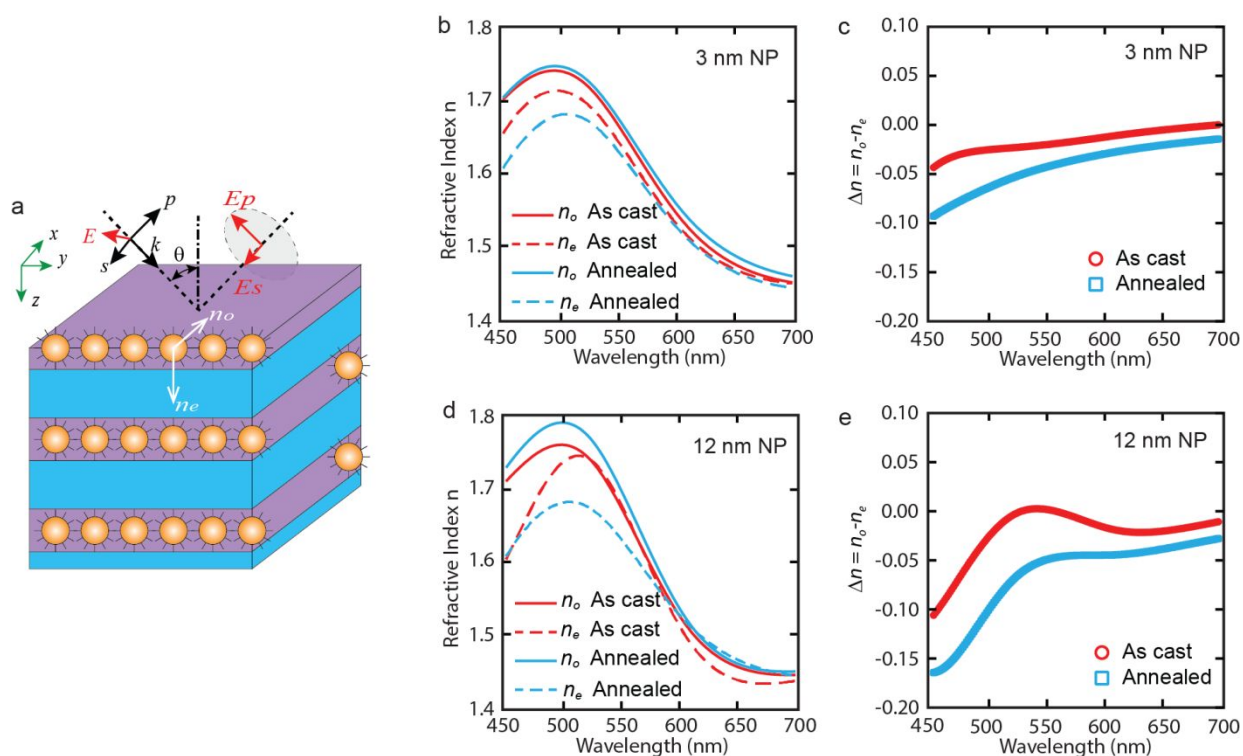


Figure S6. (a) Schematics of the ellipsometry measurements of the in-plane (n_o) and out-of-

plane (n_e) components of the refractive indices. (b, d) Ellipsometry measurements of the in-plane (n_o) and out-of-plane (n_e) components of the real refractive indices of 140 nm films containing 9 vol% of (b) 3 and (d) 12 nm Au NPs. (c, e) Difference of the out-of-plane (n_e) and in-plane (n_o) real refractive indices calculated from (b, d).

SI 6. Simulated Particle Plasmon Resonance of a Single 3 nm and 12 nm Au NP

Numerically calculated particle plasmon resonance peak of an individual Au NP in the size of 3 or 12 nm in the supramolecular matrix is 544 or 543 nm respectively.

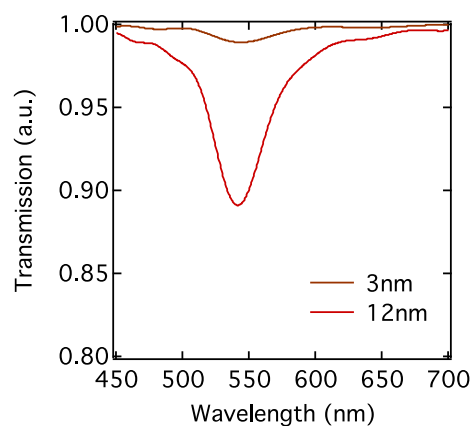


Figure S7. Simulated resonance peak of an individual Au NP in the size of 3 nm or 12 nm in the supramolecular matrix.

SI 7. In-plane Arrangement of NPs on the Surface of Supramolecular Thin Films

Thin films of Au NPs and nanocomposite on glass slides show different colors due to the different extinction properties originated from the different NP sizes and inter-particle distances.



Figure S8. Images of the thin films of Au NPs and solvent annealed nanocomposite films on glass slides.

REFERENCES

- (1) Wagner, R.; Heerklotz, L.; Kortenbruck, N.; Cichos, F. Back Focal Plane Imaging Spectroscopy of Photonic Crystals. *Appl. Phys. Lett.* **2012**, *101* (8), 081904.
- (2) Huang, C.; Yin, X.; Wang, Q.; Huang, H.; Zhu, Y. Long-Wavelength Optical Properties of a Plasmonic Crystal. *Phys. Rev. Lett.* **2010**, *104* (1), 016402.
- (3) Chen, X.; Guo, P.; He, C.; Dong, B.; Ocola, L. E.; Schaller, R. D.; Chang, R. P. H.; Sun, C. Scaling the Artificial Polariton Bandgap at Infrared Frequencies Using Indium Tin Oxide Nanorod Arrays. *Advanced Optical Materials* **2016**, *4* (12), 2077–2084.
- (4) Liu, N.; Giessen, H. Coupling Effects in Optical Metamaterials. *Angewandte Chemie International Edition* **2010**, *49* (51), 9838–9852.
- (5) Jain, P. K.; Huang, W.; El-Sayed, M. A. On the Universal Scaling Behavior of the Distance Decay of Plasmon Coupling in Metal Nanoparticle Pairs: A Plasmon Ruler Equation. *Nano Lett.* **2007**, *7* (7), 2080–2088.